

The saturation of the electron beam filamentation instability by the self-generated magnetic field and magnetic pressure gradient-driven electric field

M E Dieckmann^{1,2,3}, G Rowlands⁴, I Kourakis¹ and M Borghesi¹

1 Centre for Plasma Physics, Queen's University Belfast, Belfast BT7 1NN, U K

2 Theoretische Physik IV, Ruhr-University Bochum, 44780 Bochum, Germany

3 Department of Science and Technology (ITN), Linköping University, Campus Norrköping, 60174 Norrköping, Sweden

4 Physics Department, Warwick University, Coventry CV4 7AL, U K

E-mail: Mark.E.Dieckmann@itn.liu.se

Abstract. Two counter-propagating cool and equally dense electron beams are modelled with particle-in-cell (PIC) simulations. The electron beam filamentation instability is examined in one spatial dimension. The box length resolves one pair of current filaments. A small, a medium-sized and a large filament are considered and compared. The magnetic field amplitude at the saturation time of the filamentation instability is proportional to the filament size. It is demonstrated, that the force on the electrons imposed by the electrostatic field, which develops during the nonlinear stage of the instability, oscillates around a mean value that equals the magnetic pressure gradient force. The forces acting on the electrons due to the electrostatic and the magnetic field have a similar strength. The electrostatic field reduces the confining force close to the stable equilibrium of each filament and increases it farther away. The confining potential is not sinusoidal, as assumed by the magnetic trapping model, and it permits an overlap of current filaments (plasmons) with an opposite flow direction. The scaling of the saturation amplitude of the magnetic field with the filament size observed here thus differs from that expected from the magnetic trapping model. The latter nevertheless gives a good estimate for the magnetic saturation amplitude. The increase of the peak electrostatic and magnetic field amplitudes with the filament size implies, that the electrons heat up more and that the spatial modulation of their mean speed along the beam flow direction increases with the filament size.

PACS numbers: 52.38.Hb, 52.35.Qz, 52.65.Rr

1. Introduction

The electron beam filamentation instability (FI) generates magnetic fields in energetic astrophysical and solar flare plasmas [1, 2, 3, 4, 5]. The FI is also relevant for inertial confinement fusion (ICF) [6, 7, 8] and laboratory astrophysics [9] experiments, as well as for particle accelerators [10, 11]. The FI is driven by counter-propagating electron beams and it feeds on their mean flow energy. This contrasts the Weibel instability, which grows magnetic fields at the expense of a thermal anisotropy [12, 13, 14]. The Weibel instability and the FI can be combined to form cumulative instabilities [15]. The FI becomes important, if the beam speeds are at least mildly relativistic.

The growth and saturation of the FI can be modelled with particle-in-cell (PIC) or Vlasov codes. The FI has been investigated with a one-dimensional (1D) Vlasov code [17, 18] and with a two-dimensional (2D) PIC code [19], taking into account the ion dynamics. The impact of a flow-aligned magnetic field has been examined in Ref. [20]. PIC simulation studies have addressed the statistical properties of the FI in 1D [21] and in 2D [22, 23]. The counterstreaming electron instability has also been examined with 3D PIC simulations [24].

The probably simplest and thus widely researched plasma configuration that gives rise to the FI consists of equally dense and equally warm electron beams that have a Maxwellian velocity distribution. Their thermal velocity spread v_{th} in the rest frame of the respective beam is the same in all directions. This system can be considered in a simulation reference frame, in which both beams move into opposite directions at the non-relativistic speed modulus v_b and with $v_{th} \ll v_b$. The FI can be isolated by selecting a 1D or 2D simulation box, that is oriented orthogonally to the beam velocity vector \mathbf{v}_b . The electron velocities must be resolved in the simulation direction or plane and along the beam direction. The FI competes in reality with the two-stream modes and it can probably not be observed experimentally in an isolated form, even if the equal beam densities favor the FI over the two-stream instability [25]. However, the gained insight into the development of the isolated FI will improve the understanding of systems, in which the FI interplays with other instabilities.

The linear and nonlinear evolution of the FI driven by counter-propagating identical electron beams is qualitatively understood, at least in one spatial dimension where the filament mergers are suppressed [16]. The Refs. [14, 16, 18, 20, 21] have provided an insight into its linear and nonlinear development, which can be summarized as follows. The FI triggers the aperiodic growth of waves out of an initial perturbation (noise) with the wavevectors $\mathbf{k} \perp \mathbf{v}_b$ over a wide band of $k = |\mathbf{k}|$, where the wavenumbers k are of the order of the inverse electron skin depth. The electrons are deflected by the magnetic field perturbation, and electrons moving in opposite directions separate in space. The net current of these flow channels amplifies the initial perturbation and, thus, the tendency to form current channels. The magnetic field amplitude grows exponentially. Magnetic trapping has been identified as a possible saturation mechanism [14]. It has also been proposed [18] that the electrostatic fields, which grow during the nonlinear evolution of

the FI, may be important for the saturation. These electrostatic fields have been related to the magnetic pressure gradient [20, 21]. However, it has not yet been demonstrated quantitatively that the electrostatic fields during the quasi-linear evolution of the FI do originate from the magnetic pressure gradient. A direct comparison of the relative importance of the electric and magnetic fields for the nonlinear saturation of the FI is also lacking and this is an objective of this paper.

The length of the 1D simulation box with periodic boundaries can be selected such, that only one wave period grows. This FI evolves like that in a much larger box [21] and the saturation mechanism should thus be the same. We employ here a simulation box that resolves a single spatial period of the growing wave and we can thus compare our results to previous work [18]. We employ plasma parameters that are identical to those in Ref. [21] and resort to the distribution of the filament sizes, which is computed in that paper. We perform three simulations, in which we vary the box length. The spectrum of unstable wavenumbers of the FI is bounded at low and large wavenumbers, the latter by thermal effects [18]. The bounded k -spectrum implies in turn a maximum and a minimum filament size. We model a filament size close to the minimum value, one close to the maximum value and one, that is close to the size with the maximum probability. We compare the properties of the filaments.

This paper is structured as follows. Section 2 discusses the PIC code and the initial conditions. The results are presented in the section 3. All simulations demonstrate that the electrons are heated up orthogonally to \mathbf{v}_b , in line with previous simulations [21]. The heating is achieved by the simultaneous interaction of the electrons with the quasi-static magnetic field and the oscillatory electrostatic fields. The heating is much stronger for the larger filaments than for the small one. The magnetic field amplitude reaches a value that is in reasonable agreement with the one expected from the magnetic trapping mechanism. It does, however, not scale correctly with the filament size. A reason is that the electrostatic field modifies the potential. The force exerted by the electrostatic field in the simulation of the least turbulent small filament oscillates around a mean value that equals the magnetic pressure gradient force, confirming experimentally their connection. The fields of the two larger filaments show the same spatial correlation. The heated electrons cannot be confined by the electromagnetic field but a cooler, dense electron population remains localized, forming a plasmon. This plasmon can propagate at a sizeable fraction of the initial electron thermal speed, which contrasts the non-propagating filamentation modes out of which the plasmon forms. The plasmon maintains the net current along \mathbf{v}_b and, thus, the magnetic field. The slow extraordinary mode is pumped in the two large simulation boxes. However, the resulting growth of the discrete wave spectrum observed here, which has been reported first by Ref. [18], is a finite box effect. The results are discussed in more detail in section 4.

2. Solved equations and initial conditions

The particle-in-cell simulation method is detailed in Ref. [26]. Our code is based on the numerical scheme proposed by [27]. A PIC code approximates a phase space fluid by an ensemble of computational particles (CPs). The CPs can have a mass m_{cp} and charge q_{cp} that differs from the physical particle it represents, but the charge-to-mass ratio must be preserved. The equations, which the PIC code is solving, are

$$\nabla \times \mathbf{E} = -\frac{\partial \mathbf{B}}{\partial t}, \quad \nabla \times \mathbf{B} = \mu_0 \mathbf{J} + \mu_0 \epsilon_0 \frac{\partial \mathbf{E}}{\partial t}, \quad (1)$$

$$\nabla \cdot \mathbf{E} = \rho/\epsilon_0, \quad \nabla \cdot \mathbf{B} = 0, \quad (2)$$

$$\frac{d}{dt} \mathbf{p}_{cp} = q_{cp} (\mathbf{E}[\mathbf{x}_{cp}] + \mathbf{v}_{cp} \times \mathbf{B}[\mathbf{x}_{cp}]), \quad \frac{d}{dt} \mathbf{x}_{cp} = \mathbf{v}_{cp}, \quad (3)$$

with $\mathbf{p}_{cp} = m_{cp} \Gamma_{cp} \mathbf{v}_{cp}$. The currents $\mathbf{j}_{cp} = q_{cp} \mathbf{v}_{cp}$ of each CP are interpolated to the grid. The summation over all CPs gives the macroscopic current \mathbf{J} , which is defined on the grid. The \mathbf{J} updates the \mathbf{E}, \mathbf{B} fields through Eq.(1). The updated fields are interpolated to the position of each CP and update its position \mathbf{x}_{cp} and \mathbf{p}_{cp} through Eq.(3). This scheme is repeated over N_s time increments Δ_t .

Two equally dense beams of electrons with $q_{cp}/m_{cp} = -e/m_e$ move along the \mathbf{z} -direction. Beam 1 has the mean speed $\mathbf{v}_{b1} = v_b \mathbf{z}$ and the beam 2 has $\mathbf{v}_{b2} = -v_b \mathbf{z}$ with $v_b/c = 0.3$. Both beams have a Maxwellian velocity distribution in their respective rest frame with a thermal speed $v_{th} = (k_b T/m_e)^{0.5}$ of $v_b/v_{th} = 18$. Both beams are spatially uniform. The 1D simulation box with its periodic boundary conditions is aligned with the \mathbf{x} -direction. We thus denote positions by the scalar x . The plasma frequency of each beam with the number density n_e is $\omega_p = (e^2 n_e/m_e \epsilon_0)^{0.5}$. The total plasma frequency $\Omega_p = \sqrt{2} \omega_p$. The electric and magnetic fields are normalized to $\mathbf{E}_N = e \mathbf{E}/c m_e \Omega_p$ and $\mathbf{B}_N = e \mathbf{B}/m_e \Omega_p$ and the current to $\mathbf{J}_N = \mathbf{J}/2 n_e e c$. The physical position and time are normalized as $x_N = x/\lambda_s$ with the electron skin depth $\lambda_s = c/\Omega_p$ and $t_N = t \Omega_p$. We drop the indices N and $x, t, \mathbf{E}, \mathbf{B}, \mathbf{J}$ are specified in normalized units.

The x -direction is resolved in the three simulations by $N_g = 500$ grid cells with the length Δ_x . The phase space distributions $f_1(x, \mathbf{p})$ of beam 1 and $f_2(x, \mathbf{p})$ of beam 2 are each sampled by $N_p = 6.05 \cdot 10^7$ CPs. The total phase space density is defined as $f(x, \mathbf{p}) = f_1(x, \mathbf{p}) + f_2(x, \mathbf{p})$. The box length of run 1 is $L_1 = 2.8$, that of run 2 is $L_2 = 2$ and that of run 3 is $L_3 = 0.89$. We use L_1, L_2, L_3 to label the simulation runs. According to the size distribution in Ref. [21], we may expect that a single wave period grows in each box. The simulation L_3 captures the smallest and L_1 the largest filament that can grow with a significant probability. The simulation L_2 corresponds to a filament size close to that, which grows with the maximum probability. Multiple small filaments of a size $\approx L_3$ could grow in the larger simulation boxes. This is initially observed in the largest box L_1 , but the smaller filaments merge to give one large one.

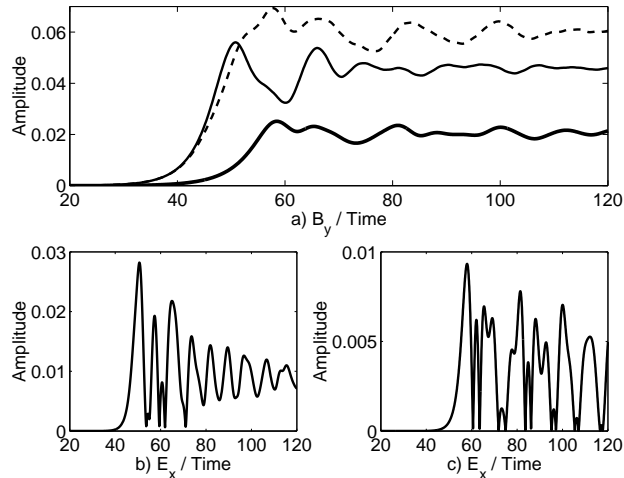


Figure 1. Field amplitudes: (a) shows the $B_y(k_1, t)$ for the box L_3 (thick solid line), the box L_2 (thin solid line) and the box L_1 (dashed line). The amplitudes grow exponentially, they saturate and oscillate around an equilibrium value. This value increases with the box size. (b) shows $E_x(k_2, t)$ for the box L_2 and (c) that for the box L_3 . The E_x component evolves towards an equilibrium value for the box L_1 (not shown) and L_2 and E_x remains oscillatory for the box L_3 .

3. Simulation results

The selected beam velocity vector $\mathbf{v}_b \parallel \mathbf{z}$ and the simulation box orientation imply, that the electrons of both beams and their micro-currents are re-distributed by the FI only along x . The charge- and current-neutral plasma is transformed into one with $J_z(x) \neq 0$. According to Eq.(1) a growth of $J_z(x)$ is coupled only into the $E_z(x)$ and $B_y(x)$ field components. This is, because the gradients along the y, z -direction vanish in the 1D geometry. Ampere's law simplifies to $dB_y/dx = J_z + \partial E_z/\partial t$. A $J_z \propto \sin(kx)$ gives a $E_z \propto \sin(kx)$ and $B_y \propto -\cos(kx)$ so that E_z and B_y will have a phase shift of 90° . The electron re-distribution leads to a space charge and thus to a $E_x(x) \neq 0$.

The $B_y(x, t)$ and $E_x(x, t)$ are Fourier transformed over space by $B_y(k_n, t) = N_g^{-1} \sum_{j=1}^{N_g} B_y(j\Delta_x, t) \exp(-ijk_n\Delta_x)$ with $k_n = 2\pi n/N_g\Delta_x$. The $E_x(x, t)$ is transformed accordingly. Figure 1 displays the time-evolution of the amplitude moduli of the dominant k_1 -mode for $B_y(k, t)$ and of the k_2 -mode for $E_x(k, t)$. The $B_y(k_1, t)$ grows exponentially at the rate $\Omega_{i,1} = \Omega_{i,2} = 0.25 \Omega_p$ until $t \approx 40$ in L_1, L_2 and at $\Omega_{i,3} = 0.22 \Omega_p$ until $t \approx 50$ in the L_3 . The maximum linear growth rate obtained from a cold fluid model is $\Omega_{i,f} = \Omega_p v_b / c\Gamma(v_b) \approx 0.29 \Omega_p$ [20]. The measured growth rate is reduced compared to $\Omega_{i,f}$ in particular for the simulation L_3 by thermal effects, which cause damping at large k . The amplitude of $B_y(k_1, t)$ saturates and remains almost constant in all simulations after $t = 80$. The saturation amplitudes are $B_y(k_1, t > 80, L_1) \approx 0.06$, $B_y(k_1, t > 80, L_2) \approx 0.045$ and $B_y(k_1, t > 80, L_3) \approx 0.02$. The magnetic trapping mechanism sets in, when $\Omega_{i,j}$ is comparable to the magnetic bounce frequency $\Omega_B = (ek_1 v_b B_y / m_e)^{1/2}$ in physical units [14]. The Ω_B for the measured growth rates above are $\Omega_B / \Omega_p = 0.2$ for

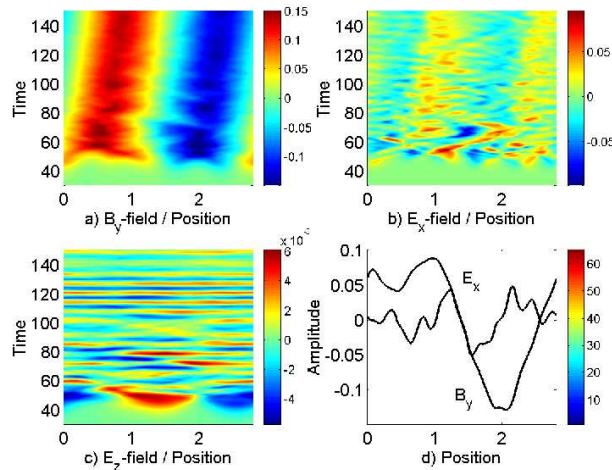


Figure 2. The field amplitudes in the box L_1 : The panels (a-c) show B_y , E_x and E_z , respectively. The B_y -amplitude reaches a steady state value, which convects slowly in space. The E_x and E_z components are oscillatory in space and time. The E_x oscillates in space twice as fast as B_y and the maxima of both are co-moving. The E_z shows a phase shift of 90° compared to B_y when the fields saturate. The B_y, E_x fields at $t = 50$ are displayed by (d) and they show a correlation only at $x \approx 1.3$.

L_1 and 0.21 for L_2 and L_3 . The agreement is excellent for the simulation L_3 , but the increase of $\Omega_{i,j}$ in the simulations L_1, L_2 compared to that in L_3 does not change Ω_B . What we find instead is, that $B_y(k_1, t > 80, L_j) \propto L_j$.

The $E_x(k_2, t)$ grows when $B_y(k_1, t)$ has reached a large amplitude and the growth rate of $E_x(k_2, t)$ is twice that of $B_y(k_1, t)$, as it has previously been reported [18, 21]. The $E_x(k_2, t)$ in the simulation L_3 oscillates between a peak value and zero, whereas we find damped oscillations around a steady state value in L_2, L_1 after $t \approx 50$. The peak amplitude of E_x in the simulation L_2 exceeds that of L_3 by the factor 3 and that in L_1 is even stronger (not shown).

3.1. Simulation L_1

The evolution of the electromagnetic fields and of the related electron phase space is now examined in more detail. Figure 2 shows the relevant fields in space and time for the simulation L_1 . It also compares the spatial distributions of $B_y(x, t)$ and $E_x(x, t)$ at the time $t = 50$, when the FI saturates. The simulation box fits one oscillation of $B_y(x, t)$ at any fixed time t after the saturation, but the more rapid oscillations along x during $40 < t < 50$ indicate that at least initially several modes are competing. Eventually, the current channels merge and form a steady state distribution in 1D [14, 21]. The magnetic field structure slowly convects to larger x . The phase speed of this structure is constant after $t = 70$ and it amounts to $\approx v_{th}/5$. The oscillations of $E_x(x, t)$ are more rapid than those of $B_y(x, t)$ for any fixed $50 < t < 55$. The maxima of $E_x(x, t)$ after $t = 70$ show a clear correlation with the structure of $B_y(x, t)$, because both convect

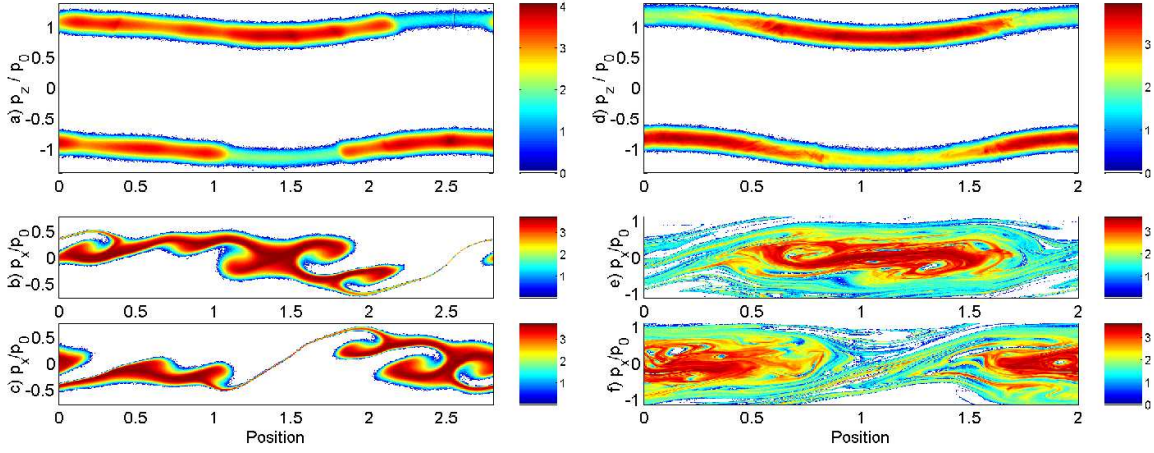


Figure 3. The 10-log of the phase space densities in units of CPs at $t = 50$ (a-c) and $t = 120$ (d-f) in the box L_1 : Panels (a,d) show the $f(x, p_z)$ with $p_0 = m_e v_b \Gamma(v_b)$. The beam temperature along p_z is unchanged and the $\langle p_z(x) \rangle_{1,2}$ are obviously modulated in space. The density oscillates by the factor $\approx 10^2$. The $f_1(x, p_x)$ is shown in (b,e) and $f_2(x, p_x)$ in (c,f). The electrons of both beams spatially separate and (e,f) reveal dense turbulent electron clouds immersed in a tenuous hot electron background, which reaches a thermal spread $\approx p_0$.

with the same phase speed. The amplitudes of $B_y(x, t = 50)$ and $E_x(x, t = 50)$ show a possible correlation only at $x \approx 1.3$. The smaller filaments are merging to the larger one at this time, complicating the interpretation of the field correlation. The $E_z(x, t)$ has the same spatial oscillation frequency as $B_y(x, t)$ for any fixed $40 < t < 55$ and their phase is shifted by the expected 90° . The amplitude of E_z is significantly lower than that of E_x . The oscillations of $E_z(x, t)$ after $t = 70$ show no pronounced structures.

Figure 3 displays the phase space densities $f_{1,2}(x, p_x)$ and $f(x, p_z)$ at the times $t = 50$ and $t = 120$. They show a significant modulation and the density maxima of both beams are shifted by $L_1/2$ at $t = 120$. The values of $f_{1,2}(x, p_x)$ and $f(x, p_z)$ vary by two orders of magnitude. The mean values $\langle p_z(x) \rangle_{1,2} = \int p_z f_{1,2}(x, \mathbf{p}) d\mathbf{p}$ for each beam show the same oscillatory modulation with x as in Ref. [21]. The $f(x, p_z)$ at $t = 50$ also shows that several filaments develop. For example, a density maximum is found at $p_x \approx 0.2$ and $p_z = p_0$ that is spatially correlated with a minimum at $p_z = -p_0$. The $p_0 = m_e v_b \Gamma(v_b)$. The absolute minima of $f_2(x, p_x)$ at $x \approx 1.5$ and of $f_1(x, p_x)$ at $x \approx 2.5$ are also not shifted by $L_1/2$. The smaller filaments cause the rapid spatial modulation of $B_y(x, t = 50)$ in Fig. 2. The electrons are heated up in p_x by the saturation of the FI from an initial thermal spread of $p_x/p_0 \approx 0.05$ to a peak value of $p_x \approx p_0$. The summation of $f(p_x) = \int f(x, \mathbf{p}) dx dp_y dp_z$ over many filaments will give a distribution, that decreases exponentially over a wide range of p_x [21].

The supplementary movie 1 shows the 10-logarithmic $f_1(x, p_x, t)$ and $f_1(x, p_z, t)$ in the simulation L_1 . It demonstrates that only the core electrons in Fig. 3 remain spatially confined. This dense core population maintains $B_y(x, t > 50)$ in Fig. 2. The structures

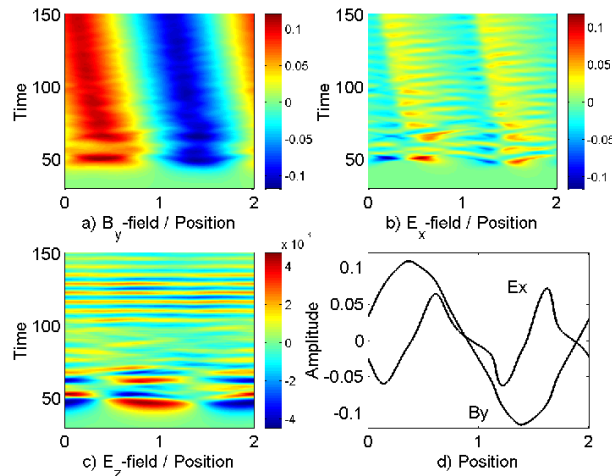


Figure 4. The field amplitudes in the box L_2 : The panels (a-c) show B_y , E_x and E_z , respectively. The B_y -amplitude reaches a steady state value, which convects slowly in space. The E_x and E_z components are oscillatory in space and time. The E_x oscillates in space twice as fast as B_y , which is obvious at $t \approx 50$. The maxima of both are co-moving. The E_z shows a phase shift of 90° compared to B_y when the fields saturate. The B_y , E_x fields at $t = 50$ are displayed by (d) and both show a clear spatial correlation. The E_x is modulated by its first harmonic.

in $f(x, p_x)$ in the movie 1, one of which occurs in Fig. 3e) at $x \approx 0.7$ and $p_x \approx 0$, resemble phase space holes [28]. The potentials of these structures contribute to the $E_x(x, t)$, causing its rapid fluctuations in Fig. 2d). These phase space holes complicate the identification of the relation between E_x , B_y in Fig. 2d) in addition to the ongoing merging of small filaments to larger ones.

3.2. Simulation L_2

We reduce now the box length from $L_1 = 2.8\lambda_s$ to $L_2 = 2\lambda_s$. The comparison of Fig. 4 with Fig. 2 reveals some similarities between the respective field evolutions. The structures in the saturated $B_y(x, t)$ and $E_x(x, t)$ fields are co-moving also in the simulation L_2 and they have here a phase speed $\approx -v_{th}/6$. The $E_z(x, t)$ and $B_y(x, t)$ have the same spatial oscillation period when they saturate at $t \approx 40$, again shifted by 90° . The $B_y(x, t)$ does not show the spatial modulations with $k > k_1$, which the $B_y(x, t)$ in Fig. 2 does prior to its saturation at $t \approx 50$. Contrary to the Fig. 2d), the $B_y(x, t = 50)$ and the $E_x(x, t = 50)$ are obviously correlated in Fig. 4d). The $E_x = 0$ whenever $(B_y dB_y/dx) = 0$, which suggests the magnetic pressure gradient as the origin of E_x . The dominant oscillations of E_x , B_y in Fig. 4d) are in the k_2 and k_1 mode, respectively. The E_x component evidences furthermore the presence of harmonics.

Figure 5 illustrates the phase space distributions $f_{1,2}(x, p_x)$ and $f(x, p_z)$ at the times $t = 50$ and $t = 120$ in the simulation L_2 . The density maxima are shifted by $L_2/2$ at both times and no further density maxima occur. The phase space structures

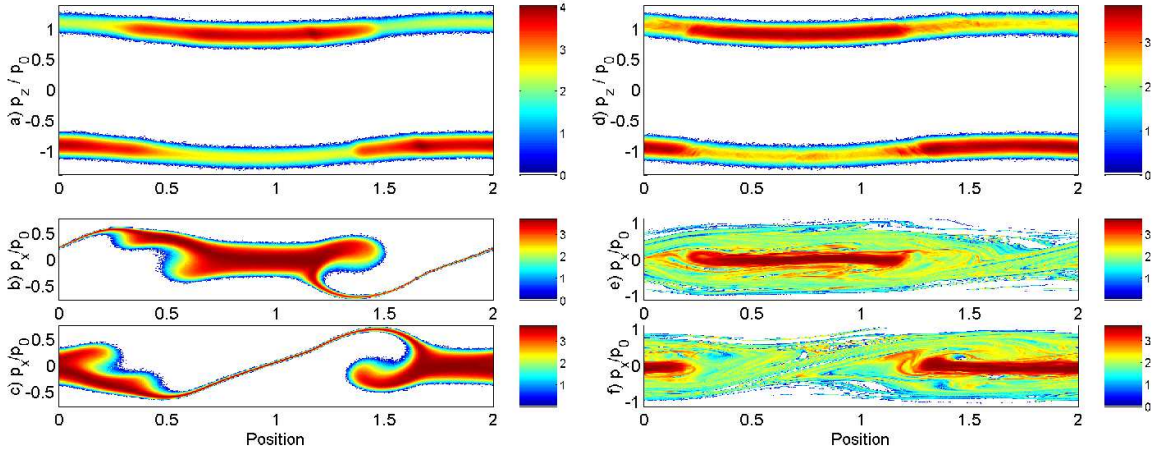


Figure 5. The 10-log of the phase space densities in units of CPs at $t = 50$ (a-c) and $t = 120$ (d-f) in the box L_2 : Panels (a,d) show the $f(x, p_z)$ with $p_0 = m_e v_b \Gamma(v_b)$. The beam temperature along p_z is unchanged and the spatial oscillations $\langle p_z(x) \rangle_{1,2}$ of the beams is weak. The density oscillates by the factor $\approx 10^2$. The $f_1(x, p_x)$ is shown in (b,e) and $f_2(x, p_x)$ in (c,f). Both beams separate in space and (e,f) reveal cool electron clouds immersed in hot electrons with a thermal spread $\approx p_0$.

of both beams at $t = 50$ reveal a high degree of symmetry, evidencing a dominant single filament. A second, independently developing filament would break such a symmetry as in the simulation L_1 . This is in line with the growth of $B_y(x, t)$ in Fig. 4 that shows only a modulation with the wavenumber k_1 . The constant slope of $E_x(0.8 < x < 1.1, t = 50)$ in Fig. 4d) corresponds to a spatially uniform distribution of $f(x, p_x)$ in Fig. 5b). The harmonics of E_x in Fig. 4d) are related to the phase space structures at the filament boundaries. The $f(x, p_x)$ at $t = 120$ shows a heated electron population similar to that in Fig. 3. The dense electron component in L_2 is, however, cooler and it shows no vortex structures. The core populations of both beams in Fig. 5e,f) are not overlapping, as the current filaments do in the Fig. 3.

The supplementary movie 2 animates in time the 10-logarithmic phase space distributions $f_1(x, p_x)$ and $f_1(x, p_z)$ of the beam 1 in the simulation L_2 . The formation of the filaments is demonstrated. The phase space evolution shows that the distribution $f(x, p_x)$ contains fewer vortices and that the vortices are spread out over a smaller interval of p_x than in the simulation L_1 . The spatial modulation of $\langle p_z(x) \rangle_1$ of the beam 1 is also less pronounced. The plasma thus appears to be less turbulent than that in L_1 , which may explain the more obvious relation between B_y and E_x in Fig. 4 compared to the Fig. 2. The spatial width of the plasmon containing the dense bulk of the electrons of $f_1(x, p_x)$ oscillates in time. The overlap of the filaments in Fig. 5e,f) is thus time dependent and related to the oscillating electrostatic field in Fig. 4b).

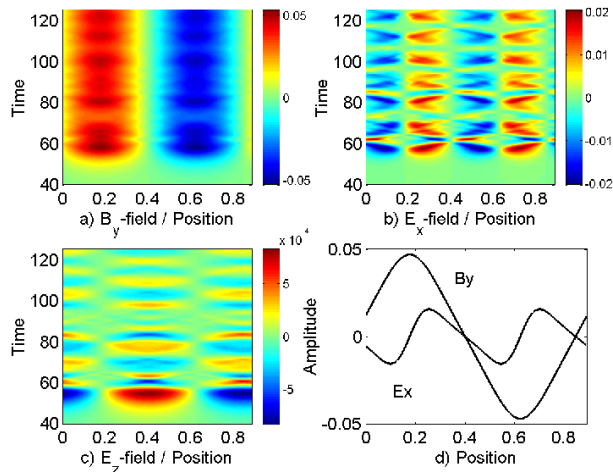


Figure 6. The field amplitudes in the box L_3 : The panels (a-c) show B_y , E_x and E_z , respectively. The B_y -amplitude reaches a steady state. The E_x and E_z components are oscillatory in space and time. The E_x oscillates in space twice as fast as B_y and both correlate well for $55 < t < 125$. The E_z shows a phase shift of 90° compared to B_y and its amplitude decreases in time. The B_y, E_x fields at $t = 56$ are displayed by (d) and we find that $E_x = 0$ when $B_y dB_y/dx = 0$.

3.3. Simulation L_3

The turbulence is reduced further, by decreasing the box length from $L_2 = 2\lambda_s$ to $L_3 = 0.89\lambda_s$. We exploit this to examine quantitatively and in more detail the relation between the electric and magnetic fields and their effect on the particle trajectories. Figure 6 displays stationary field structures. The $B_y(x, t)$ oscillates with the wavenumber k_1 in space. The E_x oscillates with the wavenumber k_2 and it is practically undamped. Both fields display a persistent correlation. The E_z component is damped in time and it is shifted by the phase 90° relative to B_y when the FI saturates. The damping of E_z does not visibly influence the B_y and E_x , suggesting that E_z is driven only during the growth phase of the FI and that it decouples upon saturation. The E_x, B_y fields show an excellent qualitative match between $E_x = 0$ and $B_y dB_y/dx = 0$ when $t = 56$.

The force of the magnetic pressure gradient on a current is expressed as

$$\mathbf{J} \times \mathbf{B} = -\nabla \cdot \mathbf{B}^2/2. \quad (4)$$

The derivatives in the y and the z directions vanish in our 1D geometry, $B_y \gg B_x, B_z$ and $J_z \gg J_x, J_y$. The magnetic pressure gradient force on the electrons can only be mediated through an electric field force along x . This electric field for the normalized electron charge -1 is then given by $E_B = -B_y dB_y/dx$. The $E_x(x, t > 56)$ oscillates in Fig. 6 in space and time between $E_x = 0$ and an extremum. The peak field moduli ≈ 0.02 are most suitable for a comparison with E_B , due to the high signal-to-noise ratio.

Figure 7a) displays the $E_x(x, t = 56)$ when the FI has just saturated and compares it with E_B . It turns out that $E_x(x) \approx 2E_B(x)$ at $t = 56$, when the peak amplitude of E_x is reached. The electric field amplitudes can be averaged over the time interval $t_1 = 56$

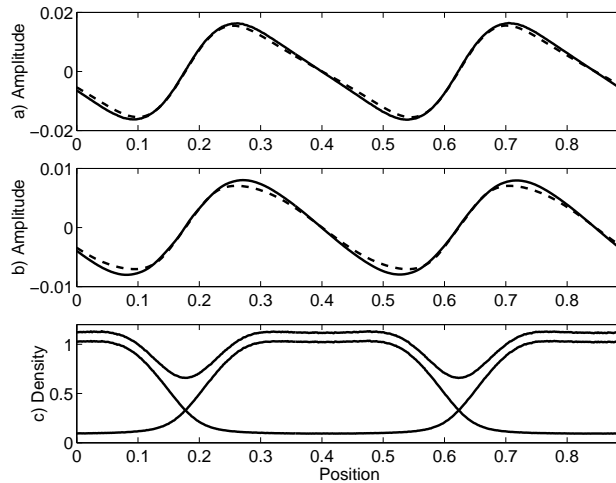


Figure 7. (a) The $E_x(x, t = 56)$ (dashed curve) and $2E_B$ (solid curve). (b) The $\tilde{E}_x(x)$ (dashed line) and \tilde{E}_B (solid line), which have been averaged over $56 < t < 125$. (c) The number densities for $t = 56$, normalized to $2n_e$, of both beams separately (beam 1 is almost confined to $0.2 < x < 0.6$) and both densities added together. The total beam density is modulated by about 30%. The density of the individual beams varies by an order of magnitude.

to $t_2 = 125$, for which the field structures do not convect and oscillate around a constant mean field, to give $\tilde{E}_x = (t_2 - t_1)^{-1} \int_{t_1}^{t_2} E_x(x, t) dt$ and $\tilde{E}_B = (t_2 - t_1)^{-1} \int_{t_1}^{t_2} E_B(x, t) dt$. The \tilde{E}_x and \tilde{E}_B match in Fig. 7b). The magnetic pressure gradient is thus the origin of the electrostatic field. The system is oscillating around the equilibrium because our initial conditions did not correspond to a steady state configuration. The same oscillations of E_x around a mean field as well as the correlation between B_y and E_x can also be observed in Fig. 2 and Fig. 4 at late times for the larger boxes. The \tilde{E}_B correlates well with the \tilde{E}_x in the simulations L_1, L_2 , although the curves do not match as accurately as in Fig. 7. This is due to the more turbulent plasma and because the convection of the structures imposes either constraints on the integration time or requires a transformation into a moving frame, the speed of which has to be estimated.

Figure 7c) shows the normalized number density distributions $n_{1,2}(x) = (2n_e)^{-1} \int f_{1,2}(x, \mathbf{p}) d\mathbf{p}$ of the individual beams and also the summed distribution $n_1(x) + n_2(x)$ at $t = 56$. The spatial oscillation period of either $n_1(x)$ or $n_2(x)$ is L_3 , while that of the $E_x(x, t = 56)$ is $L_3/2$. The phase space structures of electron phase space holes in an unmagnetized plasma would have the same periodicity as the electrostatic field [28].

Figure 8 shows the phase space distribution of the electrons in simulation L_3 at the times $t = 56, 120$. The $\langle p_z(x) \rangle_{1,2}$ are practically unchanged along the x-direction. A spatial modulation is caused by the $\mathbf{E} \times \mathbf{B}$ -drift, the speed of which is given by the product of E_x and B_y in our 1D simulations. The amplitudes of B_y and of E_x both increase according to the Figs. 2, 4 and 6 as the filaments get larger and, hence, the drift speed contribution to p_z . The amplitudes of E_x in the simulations L_1, L_2 are several times the one in the simulation L_3 and their drift electric fields $v_b B_y$ are larger. The

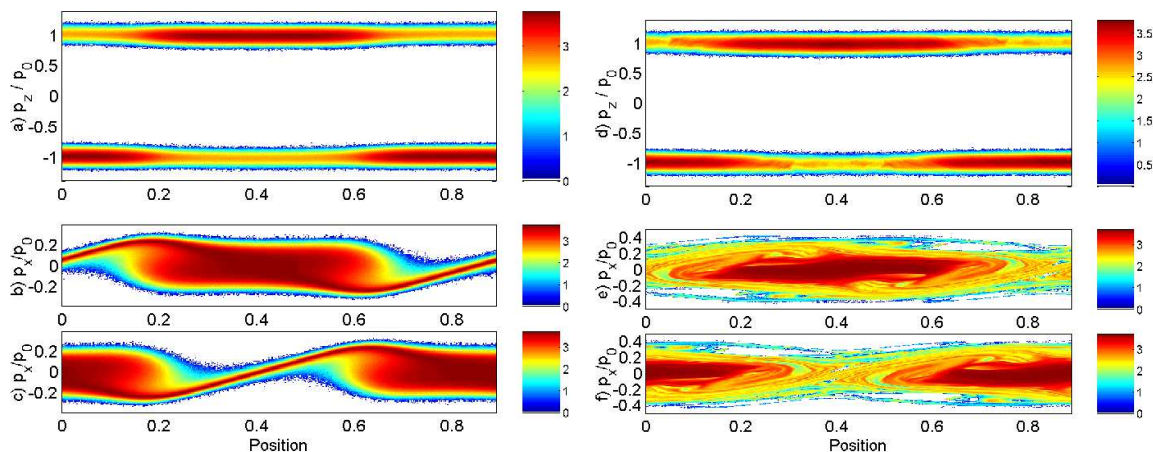


Figure 8. The 10-logarithmic phase space densities in units of CPs at $t = 56$ (a-c) and $t = 120$ (d-f) in the box L_3 : Panels (a,d) show the $f(x, p_z)$ with $p_0 = m_e v_b \Gamma(v_b)$. The temperature along p_z and the $\langle p_z(x) \rangle_{1,2}$ of each beam are unchanged. The density oscillates by the factor ≈ 10 . The $f_1(x, p_x)$ are shown in (b,e) and the $f_2(x, p_x)$ in (c,f). Both beams separate in space and (e,f) reveal cool electron clouds immersed in a tenuous electron population with a thermal spread $\approx 0.4p_0$.

simulation boxes are also longer. The electrostatic potentials in the simulations L_1, L_2 thus exceed by far that in the simulation L_3 and the electrons can reach higher kinetic energies. Consequently, the spread in p_x of the phase space distributions of both beams in the simulation L_3 is less than half of that in the simulations L_1, L_2 at $t = 120$.

The supplementary movie 3 animates in time the evolution of the 10-logarithmic distributions $f_1(x, p_x)$ and $f_1(x, p_z)$ in the simulation L_3 . The $f_1(x, p_z)$ evidences that the electrons are re-distributed along x , but not along p_z . The electron flow along x oscillates. The $f_1(x, p_x)$ after the saturation of the FI has a dense electron core, which rotates in the x, p_x -plane around $x = 0.4$. Two vortices in the dense electron core, presumably electron phase space holes, are convected with this rotating flow.

All simulations evidence that a core of cool electrons is spatially confined. Their circular phase space motion in the movies around the equilibrium points x_e with $E_x(x_e) = B_y(x_e) = 0$, for example $x_e = 0.4$ in the movie 3, furthermore reveals, that they are trapped by an electrostatic potential in the x, p_x plane. We consider the quasi-equilibrium established in the simulation L_3 after the FI has saturated. We calculate $\tilde{E}_x = (t_2 - t_1)^{-1} \int_{t_1}^{t_2} E_x(x, t) dt$ and $\tilde{B}_y = (t_2 - t_1)^{-1} \int_{t_1}^{t_2} B_y(x, t) dt$ for the simulation L_3 . We integrate both fields from $t_1 = 68$ to $t_2 = 125$, when the equilibrium is established. The weak modulation of p_z and thus v_z of the CPs in L_3 allows us to estimate the drift electric field as $\tilde{E}_D = v_b \tilde{B}_y$ and the total electric field $\tilde{E}_T = \tilde{E}_x + \tilde{E}_D$. The average potentials $\tilde{U}_j(x) = U_{0,j} + \int_0^x \tilde{E}_j(\tilde{x}) d\tilde{x}$ with the indices $j = x, D, T$ are calculated from these fields and $U_{0,j}$ is set such that $\tilde{U}_j(x_e = 0.4) = 0$. The potentials are expressed in Volts, allowing a straightforward comparison with the particle kinetic energies. The average fields and potentials are displayed by Fig. 9. The electric fields are such that \tilde{E}_x

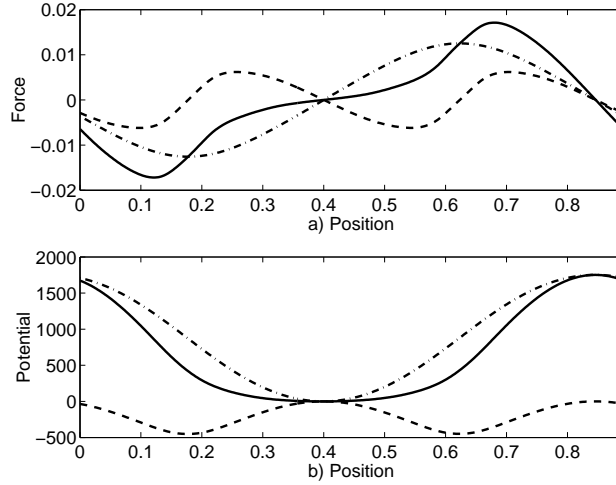


Figure 9. The fields \tilde{E}_j and the potentials \tilde{U}_j , both averaged over the time interval $68 < t < 125$: a) shows the electric field \tilde{E}_x (dashed), the $\tilde{E}_D = v_b \tilde{B}_y$ (dash-dotted) and $\tilde{E}_T = \tilde{E}_x + \tilde{E}_D$ (solid line). Positive \tilde{E}_j accelerate electrons into the negative x -direction. b) shows the potential \tilde{U}_x (dashed), \tilde{U}_D (dash-dotted) and the \tilde{U}_T (solid). The potential at $x = 0.4$ is the reference potential.

destabilizes the equilibrium position $x_e = 0.4$, because the negative $E_x(x > x_e)$ close to x_e accelerates the electron in the positive direction and the positive $E_x(x < x_e)$ close to x_e in the negative direction. The $E_D(x \approx x_e)$ is confining the electrons around $x \approx x_e$. The $|E_D| > |E_x|$ for $x \approx x_e$ and E_T is thus a confining force. However, the electron acceleration at $x \approx x_e$ is decreased and increased at larger $|x - x_e|$. This is reflected also by the potentials. The magnetic potential invoked by Ref. [14] is dominant. However, the electrostatic field flattens the bottom of the potential and steepens the walls. This modified potential results in a bouncing time of electrons that differs from that in Ref. [14]. The asymmetry of the potential close to the stable equilibrium $x_e \approx 0.4$ of the beam 1 and the stable equilibrium $x \approx 0.85$ of the beam 2 arises from the dependence of \tilde{E}_D on the beam velocity. The velocity is v_b for beam 1 and $-v_b$ for beam 2. The E_x , on the other hand, acts on both beams in the same way.

The CPs of the beam 1 should follow almost straight paths close to $x_e = 0.4$ and they should be rapidly reflected for $|x - x_e| > 0.2$. The potential difference $\Delta_U = \max(\tilde{U}_T) - \min(\tilde{U}_T) \approx 1700$ V in the simulation L_3 should trap electrons with speeds up to $\Delta_v = (2e\Delta_U/m_e)^{1/2}/v_b \approx 0.27$. This matches the momentum spread of the cool core population in movie 3 or Fig. 8. The oscillations of E_x in Fig. 6 explain the periodic release of electrons from this cool core seen in the movie 3 and the oscillatory force imposed on the electrons by E_x contributes to their heating.

The trajectories of two CPs in the confined structure of beam 1 are followed in time in Fig. 10 in order to compare their dynamics to that expected from \tilde{E}_T . The red circle denotes the time, when the CPs start interacting with the fields and the trajectories are followed until $t = 125$. The CP 1 has a low initial modulus of p_x and CP 2 a high one.

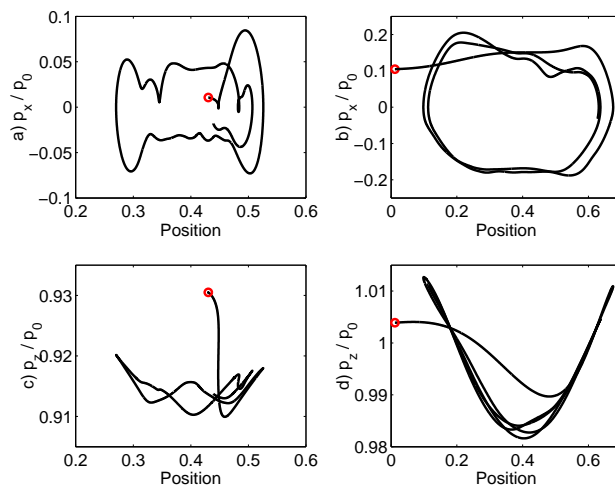


Figure 10. The particle trajectories of two selected CPs: (a,c) show the x, p_x and x, p_z diagrams of the CP 1. (b,d) show the corresponding diagrams for the CP 2. The red circle denotes the starting point of the trajectory. Both CPs follow straight paths in the x, p_x plane for $0.33 < x < 0.47$ and they are rapidly reflected outside this interval. The $E_x B_y$ drift imposes diagonal paths of the CP 2 in the x, p_z plane.

Both CPs follow straight paths in the interval $0.33 < x < 0.47$, in which \tilde{E}_T in Fig. 9 is small. The phase space path of the faster CP 2 is smoother than that of CP 1. The low speed of CP 1 implies a long crossing time of the interval with a low modulus of \tilde{E}_T and the CP 1 experiences several oscillation cycles of E_x . The simultaneous action after the saturation of the FI of the quasi-stationary B_y and the oscillatory E_x , which both vary in space, implies that the electron acceleration is a function of the position and of the phase of E_x relative to B_y . This phase-dependence results in a randomization of the particle trajectories, contributing to the plasma heating. The faster CP 2 crosses the bottom of the potential more rapidly and it experiences lower relative speed changes by the \tilde{E}_T . The particles are reflected outside the interval $0.33 < x < 0.47$ by the $|\tilde{E}_T|$. Both CPs are trapped because their speed is less than that required to overcome ΔU .

The E_z -fields are weak but not negligible. A comparison of the Figs. 2, 4 and 6 demonstrates, that its time-evolution depends on the box length. The E_z grows in all simulations prior to the saturation of the FI and its phase is shifted by 90° relative to B_y . It is thus pumped through Ampere's law by the growth of J_z . The initial, low-frequency oscillations of E_z with $k = k_1$ damp out in all simulations. They are replaced in the simulations L_1, L_2 by faster oscillations that have $k = 0$ and $k = k_1$. This is not the case for the E_z in the simulation L_3 . The power spectrum of E_z reveals the origins of the damping of the low-frequency modes and of the growth of the high-frequency modes. This power spectrum is obtained by Fourier transforming $E_z(x, t) \rightarrow E_z(k, \omega)$ over the full box and simulation time. The power spectrum $\hat{E}(k, \omega) = |E_z(k, \omega)|^2$, which we plot for the simulations L_2, L_3 in Fig. 10.

The $\hat{E}(k, \omega)$ reveals the following for the simulation L_3 . The spectrum of E_z consists

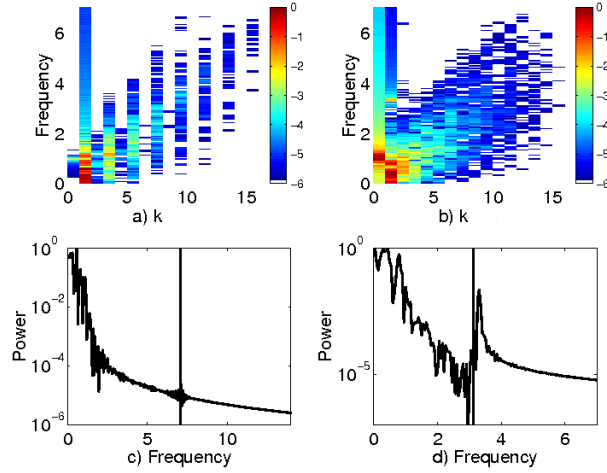


Figure 11. The 10-logarithmic power spectra of E_z , integrated over $0 < t < 125$ and normalized to their peak value. Frequencies are normalized to Ω_p . (a,c) correspond to the simulation L_3 and the k is normalized to $2\pi/L_3$. (b,d) correspond to the simulation L_2 and k is normalized to $2\pi/L_2$. (a) reveals a discrete wave spectrum in k while the spectrum in (b) is turbulent. The frequency spread is due to the growing amplitude of E_z . The frequency of the fast X-mode with $\omega \approx ck_1$ is indicated by vertical lines in (c,d). Only (d) shows a pumping of the fast X-mode.

of the fundamental mode at $k = k_1$ and of secondary waves at k_j with $j=1+2n$ and $n = 1, 2, \dots$. The modes with the $k > k_1$ are not harmonics of k_1 . They can thus not originate from a self-interaction of E_z or from a coupling of E_z with B_y , which has also $k = k_1$. It appears that E_z is interacting with the k_2 mode of E_x and, possibly, also with B_y . The power spectrum is spread out in frequency, because E_z initially grows exponentially and is thus not monochromatic. The E_z can couple to the fast extraordinary (X-)mode with the same polarization. Its frequency $\omega \approx ck$ in physical units at $k = k_1$ is high for the simulation L_3 due to the high k_1 of this simulation and no power is transferred from the low-frequency turbulence to the high-frequency fast X-mode. The transient oscillations of E_z in the simulation L_3 damp out.

As we go from L_3 to L_2 the frequency of the fast X-mode at $k = k_1$ is lowered by a factor 2.25. Figure 11 evidences that now wave energy is coupled into the fast X-mode at $k = k_1$. This pumping also transfers wave power to the mode with $k = 0$. This may be achieved by a parametric interaction of the low-frequency mode at $k = k_1$ and the high-frequency mode at $k = k_1$. The frequency spread of the initial modes implies, that it is not necessary to fulfill exactly the frequency and wavenumber conservation of the 3-wave interaction. The fast X-modes are linearly undamped, explaining the persistent high-frequency oscillations of E_z in the Figs. 2 and 4.

4. Discussion

In this work we have examined in detail the saturation of the electron beam filamentation instability (FI) with one-dimensional PIC simulations. The one-dimensional geometry implies that we can not model the FI beyond its saturation, because the filament merging is excluded [16]. However, we can readily distinguish between the electrostatic fields with their polarization vector along the simulation direction and the electromagnetic waves. The phase space distribution can also be sampled with a high statistical accuracy. We have modelled here only mobile electrons. The simulation compensates their charge by introducing an immobile positive charge background that cancels the electron charge.

The FI grows magnetic fields out of noise by a spatial separation of the currents of the, initially uniform, electron beams. A broad wavenumber spectrum is destabilized and the amplitudes of the individual filamentation modes grow aperiodically and exponentially. The magnetic field amplitude can not grow indefinitely. The magnetic amplitude saturates, once the bouncing frequency of the electrons in the magnetic potential becomes comparable to the growth rate of the instability [14]. More recently, it has been pointed out that the electrostatic fields upon saturation may not be negligible [18]. These electrostatic fields have been connected qualitatively to the magnetic pressure gradient [20, 21]. The observation, that the saturation of the FI is qualitatively unchanged by a beam-aligned magnetic field, has led to the suggestion in Ref. [20], that it is not the magnetic trapping but the electrostatic fields that quench the instability. This is, because the bouncing frequency of electrons depends on the strength of the flow-aligned magnetic field, while the electrostatic field does not; the pressure gradient of a uniform magnetic field vanishes and leaves unchanged the electrostatic field.

The electron beams in our simulations have been equally dense and cool. The beams counter-propagated at a non-relativistic speed orthogonally to the simulation direction. Picking a box length comparable to the filament size has allowed us to obtain a quasi-monochromatic wave spectrum and one pair of filaments. We have demonstrated quantitatively, that the electrostatic field is indeed driven by the magnetic pressure gradient. The initial conditions we have used here do not represent a steady state and the saturated plasma oscillates around its equilibrium state. The amplitude of the electrostatic field oscillates around the mean value, which is expected from the magnetic pressure gradient. We have demonstrated this for the small filament. Small means here, that no sub-structures can form because thermal effects [18, 29] limit the maximum unstable wavenumber. We have quantified the relative importance of the electrostatic field and of the magnetic field. The electrostatic field is comparable in strength to the drift electric field $v_b B_y$ and both are thus relevant for the saturation of the FI and for the selected plasma parameters. The electrostatic field oscillates in space twice as fast as the magnetic one. Its effect is to reduce the force on the electrons close to the equilibrium point of the respective filament and to increase it farther away from it. The effective potential obtained from a summation of the magnetic pressure-driven electrostatic field and of the drift electric field is thus not a cosine.

The electrons can move almost freely through the potential well and are reflected at a relatively thin layer, as we have demonstrated for two representative computational particles. The effective potential is not symmetric with respect to both filaments. This is, because the drift electric field depends on the beam flow direction, while the magnetic pressure-driven electric field acts on all electrons the same way. The wall of the potential that is confining one filament is located well inside the potential well of the second filament. Filaments thus remain only separated if they have opposite beam flow directions, through which they can overlap without merging. This effective potential will also accelerate ions [18]. This ion acceleration is, however, exaggerated in 1D simulations where the potential is stationary in space. The filaments merge in higher-dimensional simulations and the potentials are not longer stationary. We have thus deliberately omitted to consider ion effects.

The electrons are heated up when the potential grows and also by their simultaneous interaction with the oscillatory electric field and the steady magnetic field. A dense and spatially confined electron population (plasmon) maintains the current responsible for the magnetic field after the heating has taken place. A hot electron population overcomes the potential well and presumably contributes to the quenching of the FI, which can be suppressed by a high temperature orthogonal to the beam flow direction [29].

We have then assessed the impact of the filament size on its dynamics. The probability distribution for the filament size has been sampled using a long one-dimensional simulation box in Ref. [21]. We have examined here two other filaments, the size of which we have selected according to the probability distribution. The size of the medium filament is close to the most common size. The large filament has a size close to the maximum observed one. Larger filaments can only form, if filaments merge in higher-dimensional systems [16, 23] because the growth rate of the FI decreases, as we go to smaller wavenumbers. Long waves are then outgrown by shorter waves. The electrostatic fields of the medium and the large filament have been correlated with the magnetic field after the FI has saturated and they have oscillated around an equilibrium value. This equilibrium value is close to the magnetic pressure gradient-driven field, as for the small filament. We have not shown it, because the fit is not as accurate as for the small filament, due to the drift of the structure and the increased levels of turbulence. The sub-structure, i.e. the merging of smaller filaments in the large filament, prior to the saturation of the FI has furthermore prevented a clear correlation of the electrostatic with the magnetic field at the saturation time. Both the medium and large filaments propagated after they have saturated, even though the phase speed of the waves driven by the FI is zero. The speed has, however, been less than the initial beam thermal speed. A filament can be accelerated by the saturation of the FI. Any net momentum of the hot and untrapped electron population must be balanced by an oppositely directed net momentum of the trapped electrons. The electromagnetic fields are tied to the trapped electrons and convect with the plasmons. The direction of the convection is random. The movie in Ref. [21] shows that different convection speeds of neighboring filaments result in their spatial oscillation rather than in a convection.

The mean momentum along the beam flow direction has been spatially modulated. Our comparative study of three filament sizes has shown that the magnetic field amplitude and the electrostatic field amplitude both increase with the filament size. They modulate the mean velocity of the beam through the $\mathbf{E} \times \mathbf{B}$ -force. This modulation thus increases with the filament size, explaining the observation in Ref. [23] that trapped electrons reach increasingly higher speeds as the filaments merge.

The magnetic field has varied linearly in space over wide spatial intervals in all case studies. A magnetic field amplitude with a constant gradient results also in a magnetic pressure-driven electric field with a constant gradient. The Fourier transform over space of a curve with a constant gradient results in a power-law spectrum. This is observed also in longer- and in higher-dimensional simulation boxes [21, 23, 30].

We have examined the electric field component along the beam flow direction. Its wavenumber, the phase shift relative to the magnetic field and that it grows during the linear phase of the FI implies that it is driven through Ampere's law. These low-frequency oscillations are transient modes and they damp out. However, we have confirmed here a previous observation [18], that the fast extraordinary mode is pumped by this wave component. We could observe this only for the two large filaments. The finite box size introduces a discrete wave spectrum. The larger the box length, the lower the frequency of the electromagnetic mode. The frequency has been low enough in the large simulation boxes to absorb wave energy from the low-frequency turbulence. The discrete wave spectrum is, however, a finite box (numerical) effect.

4.1. Acknowledgments

The authors acknowledge the financial support by an EPSRC Science and Innovation award, by the visiting scientist programme of the Queen's University Belfast, by Vetenskapsrådet and by the Deutsche Forschungsgemeinschaft. The Swedish HPC2N computer center has provided the computer time and support.

References

- [1] Yang T Y B, Gallant Y, Arons J and Langdon A B 1993 *Phys. fluids B* **5** 3369
- [2] Petri J and Kirk J G 2007 *Plasma Phys. Contr. Fusion* **49** 297
- [3] Karlicky M, Nickeler D H and Barta M 2008 *Astron. Astrophys.* **486** 325
- [4] Stockem A, Lerche I and Schlickeiser R 2006 *Astrophys. J.* **651** 584
- [5] Niemiec J, Pohl M, Stroman T and Nishikawa K 2008 *Astrophys. J.* **684** 1174
- [6] Tabak M et al. 1994 *Phys. Plasmas* **1** 1626
- [7] Macchi A et al. 2003 *Nucl. Fusion* **43** 362
- [8] Campbell R B, Kodama R, Mehlhorn T A, Tanaka K A and Welch D R 2005 *Phys. Rev. Lett.* **94** 055001
- [9] Woolsey N C et al. 2001 *Phys. Plasmas* **8** 2439
- [10] Startsev E A, Davidson R C and Qin H 2007 *Phys. Plasmas* **14** 056705
- [11] Startsev E A and Davidson R C 2003 *Phys. Plasmas* **10** 4829
- [12] Weibel E S 1959 *Phys. Rev. Lett.* **2** 83
- [13] Yoon P H 2007 *Phys. Plasmas* **14** 024504

- [14] Davidson R C, Wagner C E, Hammer D A and Haber I 1972 *Phys. Fluids* **15** 317
- [15] Lazar M, Schlickeiser R and Shukla P K 2006 *Phys. Plasmas* **13** 102107
- [16] Lee R and Lampe M 1973 *Phys. Rev. Lett.* **31** 1390
- [17] Davidson R C, Hammer D A, Haber I and Wagner C E 1972 *Phys. Plasmas* **15** 317
- [18] Califano F, Cecchi T and Chiuderi C 2002 *Phys. Plasmas* **9** 451
- [19] Honda M, Meyer-ter-Vehn J and Pukhov A 2000 *Phys. Rev. Lett.* **85** 2128
- [20] Stockem A, Dieckmann M E and Schlickeiser R 2008 *Plasma Phys. Controll. Fusion* **50** 025002
- [21] Rowlands G, Dieckmann M E and Shukla P K 2007 *New J. Phys.* **9** 247
- [22] Medvedev M V, Fiore M, Fonseca R A, Silva L O and Mori W B 2005 *Astrophys. J.* **618** L75
- [23] Dieckmann M E, Lerche I, Shukla P K and Drury L O C 2007 *New J. Phys.* **9** 10
- [24] Sakai J I, Schlickeiser R and Shukla P K 2004 *Phys. Lett. A* **330** 384
- [25] Bret A, Gremillet L and Bellido J C 2007 *Phys. Plasmas* **14** 032103
- [26] Dawson J M 1983 *Rev. Mod. Phys.* **55** 403
- [27] Eastwood J W 1991 *Comput. Phys. Commun.* **64** 252
- [28] Eliasson B and Shukla P K 2006 *Phys. Rep.* **422** 225
- [29] Bret A, Firpo M C and Deutsch C 2005 *Phys. Rev. E* **72** 016403
- [30] Frederiksen J T, Hededal C B, Haugbolle T and Nordlund A 2004 *Astrophys. J.* **608** L13